Harmonic Currents Injection Strategy With Optimal Air Gap Flux Distribution for Multiphase Induction Machine

Yan Wang, Jiaqiang Yang, *Member, IEEE*, Guanghui Yang, Sheng Li, and Rongfeng Deng

***Abstract*—The proposed technique focuses on the nonsinusoidal power supply control strategy aiming to obtain the optimal air gap flux density distribution. The electrical constraints for the alignment between rotated fundamental and harmonic air gap flux are illustrated in detail. The supporting simulation is performed to analyze the misaligned angles between fundamental and harmonic air gap flux for the traditional methods. Different from traditional flux-oriented methods, the improved algorithm for harmonic currents injection is designed based on rotor flux orientated control in fundamental plane and air gap flux orientated control in harmonic planes. The synchronous and aligned control of the fundamental and harmonic air gap flux is achieved regardless of load condition. The experimental verification is implemented based on a multiphase driving platform using a seven-phase induction machine as prototype. Various scenarios are provided for the proposed control strategy comparing with the traditional ones in terms of induced electromotive force waveforms, harmonic currents, and advance angles of air gap flux. The simulated and experimental results validate the theoretical assumption and the effectiveness of the proposed method.**

***Index Terms*—Air gap flux orientated, multiphase induction machine (IM), nonsinusoidal power supply, optimal air gap flux distribution.**

NOMENCLATURE

θ	Rotation Angle of the magnetic fields.
ω	Electrical angular velocity.
δ	Angle between air gap flux and d_1-axis.
α	Angle between air gap flux and rotor flux.
C	Gain of air gap flux density.
B	Amplitude of air gap flux density.
ψ,$\vec{\psi}$	Flux linkage and its phasor quantity.
R,L	Resistance and inductance.
U,i	Voltage and current.
l,τ	Length of iron core and pole pitch.
n,p	Number of phase and number of pole pair.
N	Number of series turns per phase.
p	Differential operator.
T	Electromagnetic torque.
$\boldsymbol{M}$	Transformation matrix.
ζ_{1-4}	Angle between two phasors.

Subscripts

f	Slip component.
v	Harmonic order.
s, r, g	Stator, rotor, and air gap component.
m, σ	Magnetizing and leakage component.
d,q	Rotation coordinate system direct and quadrature axis.
1,2,3	Fundamental, third harmonic, fifth harmonic planes.

I. INTRODUCTION

MULTIPHASE machines show remarkable advantages in industrial applications of high-power, high-reliability, and high torque density, such as vessel electric propulsion, more electric aircraft, locomotive traction, and electric vehicle [1]. The inherent features of power splitting, better fault tolerance, and additional degrees of control freedom provoke the upward research in multiphase induction machine (IM) [2]. Considerable efforts have been devoted in fields of designing, modeling, and controlling of multiphase machine for several decades [3], [4]. Recent research progresses support the future widespread application prospect for multiphase machines [5]–[8].

Nonsinusoidal power supply is one of the prominent applications for multiphase IM. The enhancement for torque density and power density can be obtained through injecting harmonic currents [9]. The stable and smooth torque can be achieved by the interaction of harmonic currents and the corresponding harmonic magnetic flux. The sinusoidal fundamental magnetic flux can be effectively increased without saturating the iron core by reshaping the waveform of air gap flux quasi-trapezoidal. Benefiting from the enhanced amplitude of fundamental flux, the torque improvement of approximately 10% can be achieved when comparing with conventional three-phase machine fed by sinusoidal power supply [10], [11]. The high transient and good steady performance have been achieved for a five-phase IM supplied by the combined fundamental and third harmonic currents [12]. The robustness of the nonsinusoidal power supply controller has been studied and verified by bifurcation analysis [13].

Manuscript received November 26, 2019; revised March 5, 2020 and April 20, 2020; accepted May 26, 2020. Date of publication June 8, 2020; date of current version September 4, 2020. This work was supported in part by the National Natural Science Foundation of China under Grant 51777191 and in part by the Natural Science Foundation of Zhejiang Province under Grant LCZ19E070001. Recommended for publication by Associate Editor K. Akatsu. *(Corresponding author: Jiaqiang Yang.)*

The authors are with the College of Electrical Engineering, Zhejiang University, Hangzhou 310027, China (e-mail: herowy323@zju.edu.cn; yjq1998@163.com; guanghui@zju.edu.cn; wizardls1994@163.com; drfee163@163.com).

Color versions of one or more of the figures in this article are available online at https://ieeexplore.ieee.org.

Digital Object Identifier 10.1109/TPEL.2020.3001124

The ratios for the fundamental and harmonic flux density are optimized based on genetic algorithm to obtain the best iron utilization [14]. A comparative study for assessing the torque enhancement with different phase number was provided in [15]. A conclusion has been drawn that the torque density is not increasing along with the rise of phase number and the order of injected harmonic currents, because the width of back iron should be enlarged considering the extra stator yoke flux. In [16], it has been confirmed that the torque density and efficiency can be effectively improved by nonsinusoidal power supply under heavy load condition and it is not suitable for light load condition due to the additional harmonic magnetizing currents. The air gap and yoke flux density have been optimized simultaneously to avoid the saturation of stator back iron with nonsinusoidal power supply in [17].

Much attention has been drawn to determine the gains of the harmonic current or harmonic voltage [18]–[21], which is the critical issue to acquire the optimal enhancement in torque density and efficiency. The ratios of the injected third harmonic currents for direct-axis and quadrature-axis are both defined at constant 15% of the corresponding fundamental currents in the previous studies [18]. The strategy adopted in [19] is distinctive that the voltage-controlled method is employed to acquire the nearly trapezoidal supply terminal voltage. Different weighted combinations for the fundamental and third harmonic components are analyzed in [20], which reveals that the 13% harmonic voltage of the fundamental one is suitable for weak saturation and the harmonic ratio should be increased to around 40% for oversaturation condition. In [21], the air gap flux of a five-phase IM is optimized under the constant V/f control scheme for both the fundamental and harmonic planes, simultaneously the command third harmonic voltage is calculated based on the IM equivalent circuit. Simplification has been adopted in [21] that the induced electromotive force (EMF) waveforms are deemed approximately with the supply voltage considering the neglected stator resistance voltage drop. The amplitude and phase position of air gap flux cannot be precisely controlled by injecting the fixed ratio of harmonic currents or through the simple voltage-control method.

The improved synchronization control schemes based on the flux-oriented method have been widely adopted in recent studies [22], [23]. The relative position of the fundamental and harmonic rotating magnetic fields can be locked synchronously by restricting the fundamental and harmonic slip frequencies as equal [22]. Nevertheless, the harmonic currents algorithm is still designed with the aim of rotor flux control rather than the air gap flux control. A remedy is proposed in [23] that the advance angle for air gap flux relative to the rotor flux has been taken into account to avoid the misalignment of the fundamental and harmonic air gap flux under heavy load condition, whereas the constraint for the fundamental and harmonic slip frequencies are ignored.

A brief summary can be drawn that neither the open-loop voltage-control nor the rotor flux-oriented control scheme [9]–[22] can provide the perfect alignment of the fundamental and harmonic air gap flux. In this article, an improved solution for harmonic currents injection is presented with a novel field-oriented method. The synchronous and aligned control of the fundamental and harmonic air gap flux can be achieved irrespective of the load condition and rotor leakage flux linkage. The rest of this article is organized as follows. In Section II, the electrical constrains for the optimal control of fundamental and harmonic air gap flux are clarified based on the time-space relationship of flux phasor quantities. Afterwards, the misalignment between the fundamental and harmonic air gap flux are investigated for the traditional methods. In Section III, the proposed control scheme is elaborated to avoid the exposed drawbacks and the proposed harmonic currents injecting algorithm is deduced in steps. In Section IV, the experimental validations are carried out based on the multiphase machine driving system controlled by a dSPACE processor. The analysis and comparisons are performed in aspects of the advance angles, harmonic currents, slip frequencies, and induced EMF waveforms to further illustrate the advantage of the proposed method. Finally, Section V concludes the article.

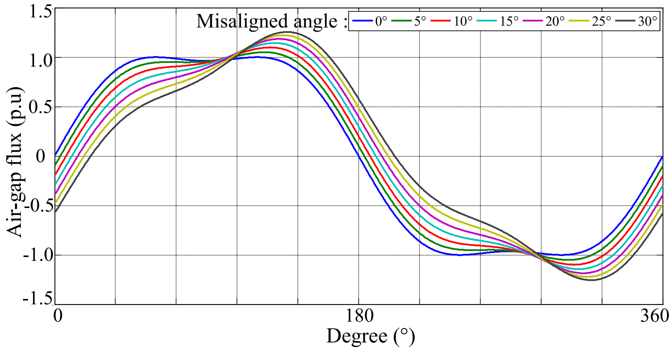

Fig. 1. Distorted waveforms of the air gap flux under different misaligned angles between fundamental and harmonic planes.

II. Phase Misalignment Analysis

In this section, the phase misalignment between the fundamental and harmonic air gap flux is analyzed for the two traditional harmonic current injecting strategies. The flux density distribution will be distorted as the axes of the fundamental and harmonic flux mismatching with each other, which is shown in Fig. 1. The disadvantages caused by this established problem have been described in Section II of [23]. The analysis results reveal that the misaligned angles give rise to the undesirable harmonic components in air gap flux and introduce the core saturation, which will further deteriorate the performance in terms of torque ripple and iron loss. The complementary analysis for flux density distribution is drawn in Fig. 2; obviously, the teeth saturation and the asymmetry of flux density distribution become severe as the misaligned angles are increasing.

A. Constraints for Optimal Air Gap Flux Distribution

The electrical constraints for the desired alignment of fundamental and harmonic air gap flux are elaborated and summarized in this part. The synthetic air gap flux density which is time-space

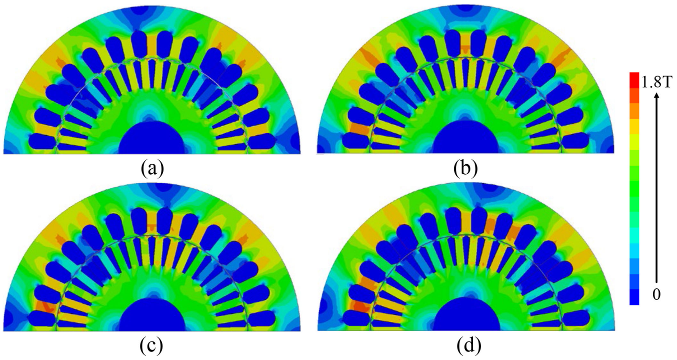

Fig. 2. Flux density distribution with different misalignment angles. (a) 0°. (b) 10°. (c) 20°. (d) 30°.

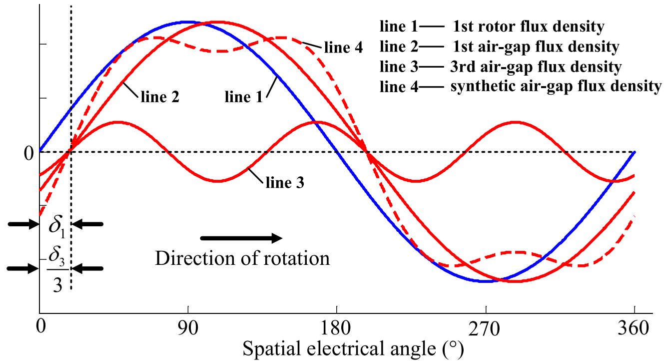

Fig. 3. Distribution of the rotor flux and air gap flux.

varied can be given as

$$B_{\mathrm{g}}(\theta,t) = C_1 B_1[\sin(\theta_1+\delta_1) + C_3\sin(\theta_3+\delta_3)] \quad (1)$$

where $C_1 = 1.155$ and $C_3 = 0.167$ are the optimized proportionality coefficients using genetic algorithm [14].

The spatial distributions for the rotor flux and air gap flux are drawn in Fig. 3. Under such circumstances, the maximum utilization of the fundamental flux can be achieved without the core saturation for any point of the distributed air gap flux density. The precise control of the relative positions and amplitudes of the rotating fundamental and harmonic air gap flux are essential for shaping the ideal waveforms of synthetic air gap magnetic field.

To keep the rotated air gap magnetic field distributing with quasi-trapezoidal waveforms, the relative position for the fundamental air gap flux and harmonic air gap flux should be synchronously locked under arbitrary rotor speed and load condition. Thus, the air gap spatial electrical angles of fundamental and harmonic planes must meet the relationship of

$$\theta_1 + \delta_1 = \frac{1}{3}(\theta_3 + \delta_3). \quad (2)$$

To obtain the smooth and stable electromagnetic torque, the rotating speeds of the fundamental and harmonic magnetic fields should be kept synchronous, which can be given as

$$\theta_1 = \frac{\theta_3}{3}. \quad (3)$$

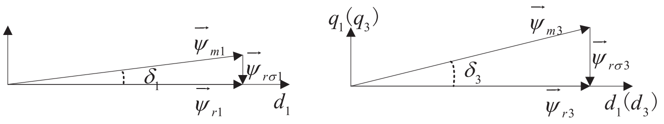

Fig. 4. Flux linkage phasor diagrams of fundamental and third harmonic planes for the traditional nonsinusoidal power supply control strategies.

The fundamental and third harmonic synchronous rotating electrical angles can be described as

$$\theta_1 = \int(\omega_r + \omega_{f1})dt \quad (4a)$$

$$\theta_3 = \int(3\omega_r + \omega_{\mathrm{f}3})dt. \quad (4b)$$

As the fundamental and harmonic rotor electrical angular velocity inherently meet the relationship of multiple of three times, thus the slip electrical angular velocity of fundamental plane and harmonic planes must follow the constraint of

$$\omega_{f3} = 3\omega_{f1}. \quad (5)$$

In addition, the advance angles for the fundamental and harmonic air gap flux in respect to the corresponding rotor flux should be satisfied with

$$\delta_3 = 3\delta_1. \quad (6)$$

The amplitudes of the fundamental and third harmonic air gap flux linkage can be expressed as

$$\left|\vec{\psi}_{m1}\right| = N \cdot B_1 \cdot l \cdot \tau \quad (7a)$$

$$\left|\vec{\psi}_{m3}\right| = N \cdot C_1 \cdot C_3 \cdot B_1 \cdot l \cdot \frac{\tau}{3}. \quad (7b)$$

Therefore, the constraint for amplitudes can be derived as

$$\left|\vec{\psi}_{m3}\right| = C_1 \cdot \frac{C_3}{3} \cdot \left|\vec{\psi}_{m1}\right|. \quad (8)$$

The optimal air gap flux distribution can be obtained under arbitrary load condition if the three constraints (5), (6), and (8) are achieved simultaneously.

B. Traditional Control Strategies

For the voltage-controlled frames, the impedance voltage drop of stator winding is usually disregarded and the control target is focused on the supply voltage rather than the induced EMF [19]–[21]. For the current closed-loop control schemes, the rotor leakage flux is usually neglected and the attention is toward the rotor flux control rather than the air gap flux control, as described in [9], [16], and [22]. However, the ideal air gap magnetic field distribution is difficult to obtain under heavy load condition. Two conventional nonsinusoidal power supply strategies [22], [23] based on rotor flux-oriented control scheme are taken into discussion.

The fundamental and harmonic flux phasor diagrams are drawn in Fig. 4 and the rotor flux orientated control (RFOC) is applied on both the fundamental and harmonic planes. The

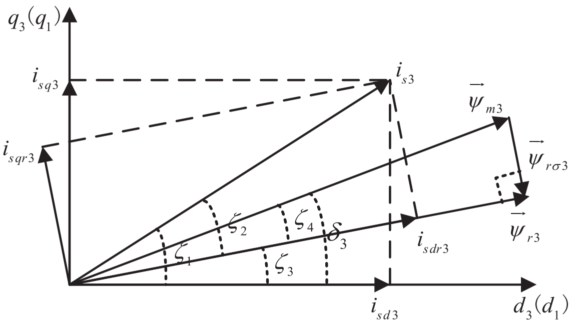

Fig. 5. Modified flux and current phasor diagram for traditional method II.

d-axis and q-axis harmonic currents for traditional method I are given by

$$i_{sd\upsilon} = \frac{C_\upsilon}{\upsilon}\frac{L_{m1}}{L_{m\upsilon}} i_{sd1} \tag{9a}$$

$$i_{sq\upsilon} = C_\upsilon \frac{L_{m1}}{L_{m\upsilon}}\frac{L_{r\upsilon}}{L_{r1}}\frac{R_{r1}}{R_{r\upsilon}} i_{sq1}. \tag{9b}$$

The slip frequencies of each plane are restricted as equal, so that the fundamental and harmonic rotating magnetic fields can be controlled synchronously. However, it has been explained that the constraint for the advance angles (6) cannot be guaranteed, which may induce serious misalignment between the fundamental and harmonic air gap magnetic fields under heavy load conditions [23]. The d-axis and q-axis harmonic currents for traditional method II are expressed as

$$i_{sd\upsilon} = \frac{L_{r\upsilon}\psi_{m\upsilon}}{L_{m\upsilon}L_{r\sigma\upsilon}} \sin\left(\upsilon \cdot \sin^{-1}\left(\frac{L_{m1}L_{r\sigma1}i_{sq1}}{L_{r1}\psi_{m1}}\right)\right) \tag{10a}$$

$$i_{sq\upsilon} = \frac{\psi_{m\upsilon}}{L_{m\upsilon}} \cos\left(\upsilon \cdot \sin^{-1}\left(\frac{L_{m1}L_{r\sigma1}i_{sq1}}{L_{r1}\psi_{m1}}\right)\right). \tag{10b}$$

The control target has been converted to the air gap flux in traditional method II. However, the flux-oriented method still follows the flux phasor relationship drawn in Fig. 4. The constraints for advance angle (6) and amplitude of air gap flux (8) are both considered, while the constraint for slip frequency (5) was neglected, which makes the theoretical derivation reasonable only under no-load condition. The two traditional methods cannot meet the three constrains simultaneously.

The command synchronous rotating speed of third harmonic plane is given based on the fundamental one [23]. Hence, the fundamental and harmonic slip frequencies are forced to equality due to the same rotor speed. It should be claimed that the rotor flux is oriented based on the d_3-axis shown in Fig. 4 while calculating the third harmonic slip frequencies. However, the actual third harmonic rotor flux will deviate from d_3-axis under load condition. The constraint (6) for advance angle may be no longer valid due to the change in the actual flux phasor diagram. It is necessary to identify the actual position of the harmonic air gap flux for the following analysis. The modified phasor diagram for traditional method II is drawn in Fig. 5. Based on the precondition of the relationship between fundamental and harmonic slip angular frequencies (11), the actual third harmonic advance angle δ_3 shown in Fig. 5 can be derived through the following:

TABLE I
MAIN PARAMETERS OF THE PROTOTYPE

Phase number	7	Pole number	4
Rated voltage (rms)	110V	Rated current (rms)	12A
Rated flux	0.48Wb	Rated magnetizing current	3.6A
Rated speed	1460rpm	Number of turns	76
Number of stator slots	28	Number of rotor slots	38

TABLE II
PARAMETERS OF SEVEN-PHASE IM USED FOR MODELING AND DRIVING

Parameters category	1th plane	3th plane	5th plane
Magnetizing inductance (mH)	129.8	15.3	5.9
Stator leakage inductance (mH)	6.5	4.2	3.9
Rotor leakage inductance (mH)	6.0	3.5	3.2
Stator resistance (Ohm)	0.51	0.51	0.51
Rotor resistance (Ohm)	0.39	0.33	0.31

$$\omega_{f3} = 3\omega_{f1} = \frac{i_{sq3r}}{i_{sd3r}}\frac{R_{r3}}{L_{r3}} \tag{11}$$

$$\zeta_1 = \arctan\left(\frac{i_{sq3}}{i_{isd3}}\right) \tag{12}$$

$$\zeta_2 = \arctan\frac{i_{sq3r}}{i_{sd3r}} = \arctan\left(3\omega_{f3}\frac{L_{r3}}{R_{r3}}\right) \tag{13}$$

$$i_{s3} = \sqrt{i_{sd3}^2 + i_{sq3}^2} \tag{14}$$

$$i_{sd3r} = i_{s3}\cos\zeta_2, i_{sq3r} = i_{s3}\sin\zeta_2 \tag{15}$$

$$\psi_{r3} = L_{r3}i_{sd3r}, \psi_{r\sigma3} = L_{r\sigma3}i_{sq3r} \tag{16}$$

$$\zeta_4 = \arctan\left(\frac{\psi_{r\sigma3}}{\psi_{r3}}\right) \tag{17}$$

$$\delta_3 = \zeta_3 + \zeta_4 = (\zeta_1 - \zeta_2) + \zeta_4. \tag{18}$$

C. Simulation Analysis

The deviation of the phase angle between fundamental and harmonic air gap flux was discussed for the two traditional approaches. A self-designed seven-phase IM with concentrated and full-pitch windings is regarded as prototype. The machine specifications are presented in Table I. The resistance and inductance parameters of the seven-phase IM used for modeling and experiment are listed in Table II, which are obtained through the analytical method [24] and the offline estimation [25].

Under ideal no-load condition, the rotating air gap flux of fundamental and harmonic planes will be naturally aligned with each other as the rotor leakage flux is zero. The advance angles of air gap flux δ_1 and δ_3 depend on the load torque and rotor leakage flux. The comprehensive analysis for the misaligned angles is performed with the extended range of load torque and rotor leakage inductance. It must be noted that the rotor leakage inductance is usually deemed as constant for the

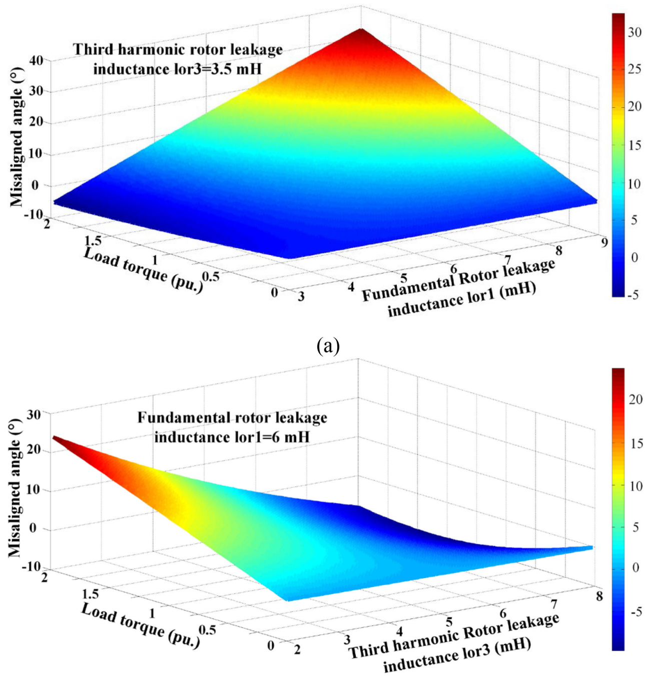

(a)

(b)

Fig. 6. Misaligned angle under extended range of load torque and rotor leakage inductance for traditional method I. (a) Variational fundamental rotor leakage inductance. (b) Variational third harmonic rotor leakage inductance.

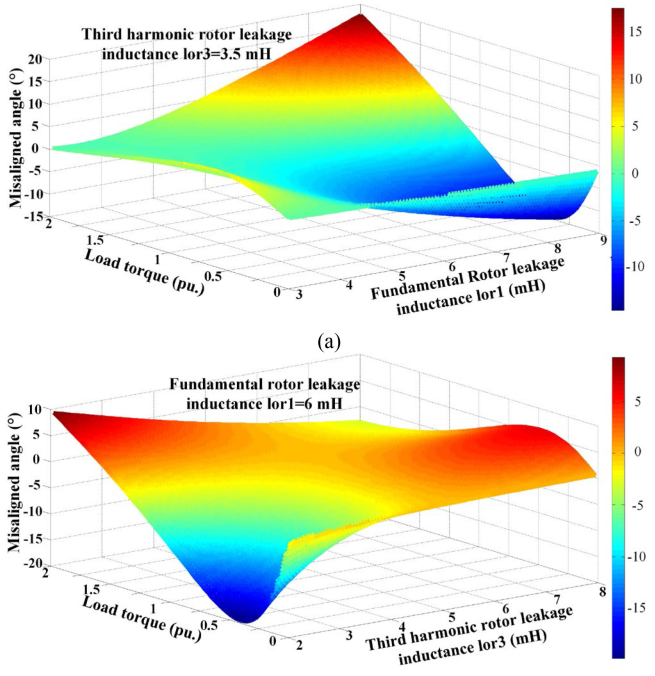

(a)

(b)

Fig. 7. Misaligned angle under extended range of load torque and rotor leakage inductance for traditional method II. (a) Variational fundamental rotor leakage inductance. (b) Variational third harmonic rotor leakage inductance.

specific machine, therefore the various rotor leakage inductance is utilized to explore the misaligned angles beyond the limitation of the prototype machine.

The misaligned angles for different combinations of leakage inductance and load torque are scanned for traditional method I. In Fig. 6(a), the rotor leakage inductance of third harmonic plane is fixed at the nominal value 3.5 mH and the fundamental one varies from 3 to 9 mH. Whereas in Fig. 6(b), the fundamental rotor leakage inductance is fixed at the nominal value 6 mH and the third harmonic one varies from 2 to 8 mH. The misaligned angles become large as the load torque increases, meanwhile the situation becomes serious with the rising of the difference between fundamental and harmonic rotor leakage inductance. The misaligned degree is relatively slight when the fundamental and third harmonic rotor leakage inductances are close to each other.

The scanned misaligned angles for traditional method II are depicted in Fig. 7. The fundamental air gap flux may be ahead of or lag the harmonic one at different load conditions. For traditional method I, it shows linear characteristic for the relationship between misaligned angle and load torque, while it becomes nonlinear for traditional method II. The misaligned angles may be larger for the light load than the heavy load conditions. The deviation between the fundamental and harmonic air gap flux may disappear or be negligible with some specific combinations of load torque and rotor leakage inductance, whereas the deviation cannot be tolerated for most conditions. The ideal alignment for the fundamental and harmonic air gap flux cannot be achieved for arbitrary load condition and arbitrary combination of the fundamental and harmonic rotor leakage inductance.

III. PROPOSED CONTROL STRATEGY

In this section, the harmonic currents injecting strategy is reconstructed based on the novel flux-oriented scheme. According to the spatial distribution of air gap flux shown in Fig. 3, the axis of fundamental rotor flux (d_1-axis) should be deemed as the referenced axis while calculating the advance angle for both the fundamental and harmonic air gap flux. If the d-axis for fundamental and third harmonic planes is both rotor field-oriented, the d_1-axis and d_3-axis are along with the same direction as described in Fig. 4. The advance angle of air gap flux varies with the load current, so that it is difficult to meet constraint (6) under arbitrary load torque based on such field-oriented method.

To avoid the contradiction when the three constrains (5), (6), and (8) are expected to achieve simultaneously based on the traditional rotor flux-oriented frame, the air gap flux-oriented method is applied on the harmonic planes in the proposed method. The proposed flux linkage phasor diagrams for the fundamental and third harmonic planes are drawn in Fig. 8. The d_1-axis is fixed on the fundamental rotor flux axis, while the d_3-axis is fixed on the third harmonic air gap flux axis. The third harmonic advance angle δ_3 is determined based on the fundamental one δ_1, which depends on the load condition and rotor leakage flux. The harmonic currents injecting algorithm can be deduced based on the proposed flux-oriented method with the following equations (19)–(39).

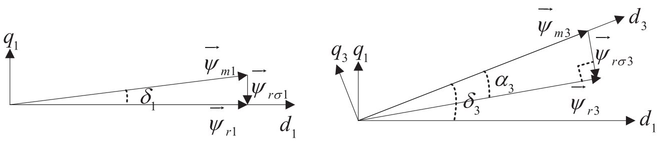

Fig. 8. Flux linkage phasor diagrams of fundamental and third harmonic planes for the proposed nonsinusoidal power supply control strategy.

The derivations of the proposed method are based on the two-phase rotating coordinate system. The stator and rotor flux linkage equations of fundamental plane can be written as

$$\psi_{sd1} = L_{s1}i_{sd1} + L_{m1}i_{rd1} \tag{19a}$$

$$\psi_{sq1} = L_{s1}i_{sq1} + L_{m1}i_{rq1} \tag{19b}$$

$$\psi_{rd1} = L_{m1}i_{sd1} + L_{r1}i_{rd1} \tag{19c}$$

$$\psi_{rq1} = L_{m1}i_{sq1} + L_{r1}i_{rq1}. \tag{19d}$$

The fundamental air gap flux linkage can be written as

$$\psi_{md1} = L_{m1}(i_{sd1} + i_{rd1}) \tag{20a}$$

$$\psi_{mq1} = L_{m1}(i_{sq1} + i_{rq1}). \tag{20b}$$

The *d*-axis and *q*-axis rotor currents of fundamental plane under steady-state condition can be given as

$$i_{rd1} = 0 \tag{21a}$$

$$i_{rq1} = -\frac{L_{m1}}{L_{r1}}i_{sq1}. \tag{21b}$$

Substituting the rotor currents (21a) and (21b) into the fundamental air gap flux linkage (20a) and (20b) yields

$$\psi_{md1} = L_{m1}i_{sd1} \tag{22a}$$

$$\psi_{mq1} = L_{m1}\left(1 - \frac{L_{m1}}{L_{r1}}\right)i_{sq1}. \tag{22b}$$

Therefore, the amplitude of fundamental air gap flux linkage can be obtained as

$$\left|\vec{\psi}_{m1}\right| = \sqrt{\psi_{md1}^2 + \psi_{mq1}^2} = L_{m1}\sqrt{i_{sd1}^2 + \left(1 - \frac{L_{m1}}{L_{r1}}\right)^2 i_{sq1}^2}. \tag{23}$$

Meanwhile, the air gap flux linkage equations in third harmonic plane can be given by

$$\psi_{md3} = L_{m3}(i_{sd3}+i_{rd3}) \tag{24a}$$

$$\psi_{mq3} = L_{m3}(i_{sq3}+i_{rq3}). \tag{24b}$$

As the rotating frame of third harmonic plane is air gap flux oriented, the *d*-axis component is the air gap flux linkage and the *q*-axis component is zero, which can be written as

$$\psi_{md3} = \psi_{m3} \tag{25a}$$

$$\psi_{mq3} = 0. \tag{25b}$$

Combining (24b) and (25b) yields the relationship of the stator and rotor *q*-axis currents in third harmonic plane

$$i_{sq3} = -\,i_{rq3}. \tag{26}$$

The rotor voltage equations of third harmonic plane can be written as

$$\mathrm{U}_{rd3} = R_{r3}i_{rd3} + p\psi_{rd3} - \omega_{f3}\psi_{rq3} = 0 \tag{27a}$$

$$\mathrm{U}_{rq3} = R_{r3}i_{rq3} + p\psi_{rq3} + \omega_{f3}\psi_{rd3} = 0. \tag{27b}$$

The rotor flux linkage equations of third harmonic plane can be given by

$$\psi_{rd3} = L_{m3}i_{sd3} + L_{r3}i_{rd3} \tag{28a}$$

$$\psi_{rq3} = L_{m3}i_{sq3} + L_{r3}i_{rq3}. \tag{28b}$$

Substituting the rotor flux linkage (28a) and (28b) into the rotor voltage (27a) and (27b) yields

$$R_{r3}i_{rd3} - \omega_{f3}L_{m3}i_{sq3} - \omega_{f3}L_{r3}i_{rq3} = 0 \tag{29a}$$

$$R_{r3}i_{rq3} + \omega_{f3}L_{m3}i_{sd3} + \omega_{f3}L_{r3}i_{rd3} = 0. \tag{29b}$$

Substituting (5) and (26) into the rotor flux linkage (29a) and (29b) yields

$$R_{r3}i_{rd3} - 3\omega_{\mathrm{f1}}L_{m3}i_{sq3} + 3\omega_{f1}L_{r3}i_{sq3} = 0 \tag{30a}$$

$$-\,R_{r3}i_{sq3} + 3\omega_{f1}L_{m3}i_{sd3} + 3\omega_{f1}L_{r3}i_{rd3} = 0 \tag{30b}$$

where

$$\omega_{f1} = \frac{L_{m1}i_{sq1}}{T_{r1}\psi_{r1}}. \tag{31}$$

Simplifying (30a) and (30b), the stator and rotor *d*-axis currents of third harmonic plane can be obtained as

$$i_{rd3} = -\frac{3\omega_{f1}l_{r\sigma3}i_{sq3}}{R_{r3}} = Xi_{sq3} \tag{32a}$$

$$i_{sd3} = \frac{9\omega_{\mathrm{f1}}^2 L_{r3}l_{r\sigma3} + R_{r3}^2}{3\omega_{f1}L_{m3}R_{r3}}i_{sq3} = Yi_{sq3} \tag{32b}$$

where

$$X = -\frac{3\omega_{f1}l_{r\sigma3}}{R_{r3}}, Y = \frac{9\omega_{\mathrm{f1}}^2 L_{r3}l_{r\sigma3} + R_{r3}^2}{3\omega_{f1}L_{m3}R_{r3}}. \tag{33}$$

Afterwards, the amplitude of air gap flux linkage for third harmonic plane can be acquired as

$$\left|\vec{\psi}_{m3}\right| = \psi_{md3} = L_{m3}(i_{sd3} + i_{rd3}) = L_{m3}(X + Y)i_{sq3}. \tag{34}$$

Thereupon, according to the constraint for air gap flux linkage amplitude (8), the reconstructed *d*-axis and *q*-axis stator currents of third harmonic plane can be derived as

$$i_{sq3} = \frac{\mathrm{C}_1\mathrm{C}_3}{3}\frac{L_{m1}\sqrt{i_{sd1}^2 + (1 - \frac{L_{m1}}{L_{r1}})^2 i_{sq1}^2}}{L_{m3}(X + Y)} \tag{35a}$$

$$i_{sd3} = \frac{\mathrm{C}_1 C_3}{3}\frac{L_{m1}\sqrt{i_{sd1}^2 + \left(1 - \frac{L_{m1}}{L_{r1}}\right)^2 i_{sq1}^2}}{L_{m3}(X + Y)}Y. \tag{35b}$$

As depicted in Fig. 8, the d_3-axis leads d_1-axis by the advance angle of δ_3, so that the Park transformation matrices for fundamental and third harmonic planes can be written as

$$\boldsymbol{M}_1 = \begin{bmatrix} \cos(\theta_1) & \sin(\theta_1) \\ -\sin(\theta_1) & \cos(\theta_1) \end{bmatrix} \tag{36}$$

$$\boldsymbol{M}_3 = \begin{bmatrix} \cos(\theta_3+\delta_3) & \sin(\theta_3+\delta_3) \\ -\sin(\theta_3+\delta_3) & \cos(\theta_3+\delta_3) \end{bmatrix}. \tag{37}$$

To meet the constraint (6), the Park transformation matrix for third harmonic plane should be modified to

$$\boldsymbol{M}_3 = \begin{bmatrix} \cos(\theta_3+3\delta_1) & \sin(\theta_3+3\delta_1) \\ -\sin(\theta_3+3\delta_1) & \cos(\theta_3+3\delta_1) \end{bmatrix} \tag{38}$$

where

$$\delta_1 = \arcsin\left(-\frac{L_{m1} l_{r1} i_{sq1}}{L_{r1}\psi_{m1}}\right). \tag{39}$$

The electromagnetic torque based on the constant amplitude transformation for the fundamental plane which is rotor flux-oriented can be given as

$$T_1 = n\cdot P\cdot \frac{L_{m1}}{L_{r1}}\cdot\psi_r\cdot i_{sq1} = n\cdot P\cdot\frac{{L_{m1}}^2}{L_{r1}}\cdot i_{sd1}\cdot i_{sq1}. \tag{40}$$

Whereas the electromagnetic torque for the harmonic planes which is air gap flux-oriented can be deduced as

$$T_\upsilon = n\cdot \upsilon P\cdot\psi_{g\upsilon}\cdot i_{sq\upsilon} = n\cdot\upsilon P\cdot L_{m\upsilon}\cdot i_{mg\upsilon}\cdot i_{sq\upsilon} \tag{41}$$

where the equivalent magnetizing current for the air gap flux is

$$i_{mg\upsilon} = i_{sd\upsilon} + i_{rd\upsilon}. \tag{42}$$

The core saturation can be limited more effectively for the air gap flux orientated control (AFOC) than RFOC. The air gap field orientation is not usually applied for high performance vector control due to relatively complicated control scheme and nonlinear torque verse speed characteristics. The main idea of the proposed strategy is that the fundamental plane is based on RFOC which contributes most of the output torque, while the harmonic plane is based on AFOC which limits the amplitude of air gap magnetic flux. The rotor flux of the fundamental and harmonic planes is no longer along the same direction under load condition for the proposed control strategy.

IV. EXPERIMENTAL VERIFICATION

A. System Configuration

The experimental platform for the seven-phase IM driving system is depicted in Fig. 9. The overall system is composed by the self-designed seven-phase IM, alternating current servo loader, dSPACE controller, multiphase inverter, and dc power supply. The multiphase half-bridge inverter is constructed by several groups of IGBT device, filter capacitors, current and voltage sensors, etc. The information for the feedback currents and feedback speed are measured by sensors and then recorded through the upper computer of dSPACE with the sampling frequency of 10 kHz.

A search coil is embedded in the surface of stator slot wedge to acquire the waveform of air gap induced EMF, which is displayed in Fig. 10. The waveform of the induced EMF distributed in time-domain corresponds identically with the spatially distributed air gap magnetic field [19], so that it can be utilized to evaluate the performance in terms of the air gap magnetic field distribution. The block diagram for nonsinusoidal power supply control is depicted in Fig. 11. The conventional control scheme which is based on the speed outer loop and current inner loop are employed to carry out the experimental validation. The third harmonic currents injecting methods for the traditional methods and the proposed method are based on (9), (10), and (35), respectively, while the fifth harmonic currents are restricted to zero. The advance angles, slip frequencies, and RMS of phase current are calculated using the feedback currents to perform the analysis and comparisons.

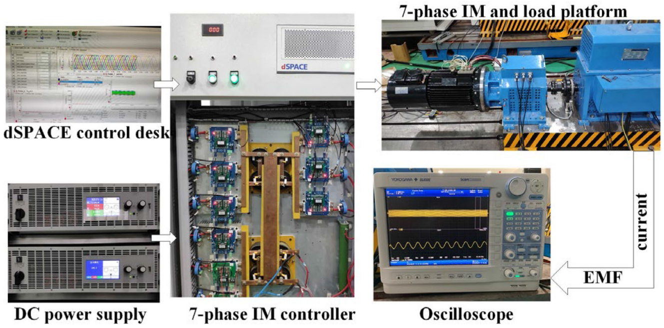

Fig. 9. Seven-phase IM driving platform.

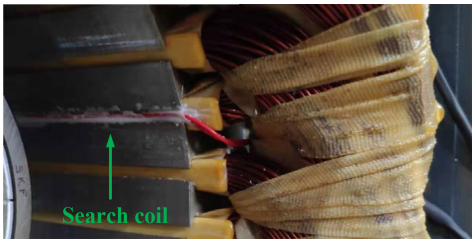

Fig. 10. Position of the search coil.

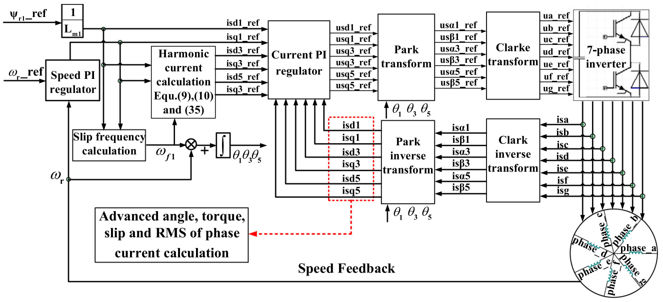

Fig. 11. Block diagram for performing the nonsinusoidal power supply control.

B. Experimental results

The transient response and steady performance are compared for the traditional and proposed methods. The speed and torque curves are depicted in Fig. 12. The machine is operated under no-load condition during the first two seconds (2 s) with the referenced speed of 1000 rpm and the step load torque of 35 Nm

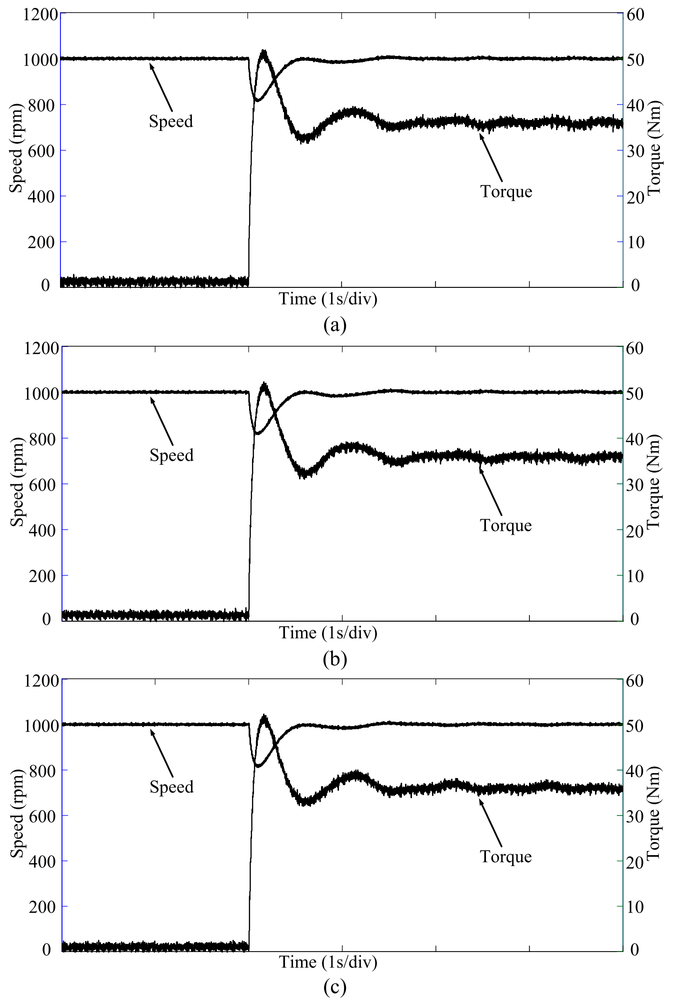

(a)

(b)

(c)

Fig. 12. Torque and speed performance. (a) Traditional method I. (b) Traditional method II. (c) Proposed method.

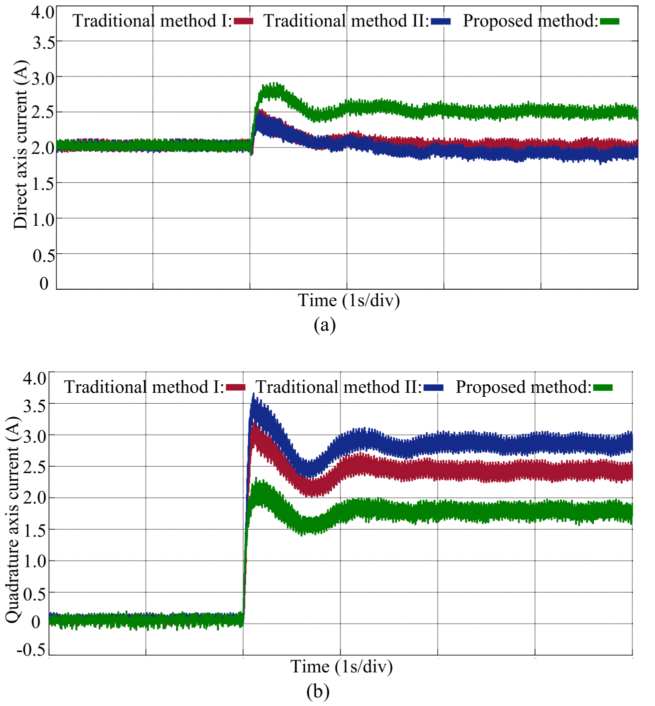

(a)

(b)

Fig. 13. Comparison for the harmonic currents of the traditional and proposed methods. (a) *d*-axis of currents. (b) *q*-axis of currents.

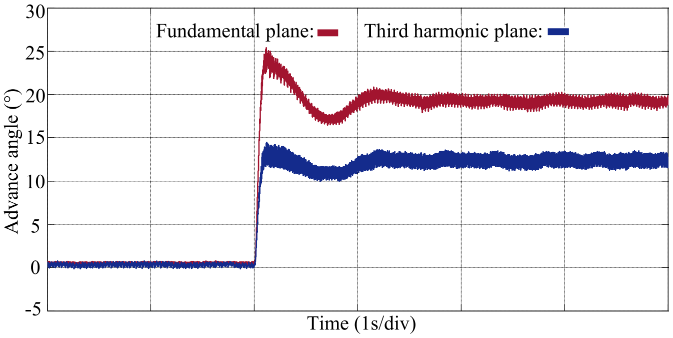

Fig. 14. Comparison for the fundamental and harmonic advance angles of traditional method I.

(rated torque) is applied at 2 s. There is no distinct difference for the three methods and it can be explained that the fundamental plane contributes most of torque. The algorithms applied on fundamental plane are the same for the three methods, while the differences reflect on the harmonic currents injecting strategies.

The comparisons for the *d*-axis and *q*-axis harmonic currents for both the traditional and proposed methods are shown in Fig. 13. Under no-load condition, the *d*-axis harmonic currents are equivalent for the three strategies and the *q*-axis harmonic currents are zero. The *d*-axis and *q*-axis harmonic currents under rated load condition are different for the traditional and proposed schemes due to the different harmonic currents injecting algorithms. As the d_3-axis is leading the d_1-axis under heavy load condition for the proposed strategy, the *d*-axis harmonic current is larger than the traditional ones and the *q*-axis harmonic current is smaller than the traditional ones.

For traditional method I, the fundamental and third harmonic advance angles between the air gap flux and rotor flux are calculated from no-load to rated load conditions, which are shown in Fig. 14. For no-load condition, the advance angles are nearly zero as the load current is approximately zero. The step change for the advance angles is occurred at 2 s as the rated load torque is implemented. The fundamental advance angle is ahead of the third harmonic one by about 6.9° electrical angle, which induces the misalignment between the fundamental and harmonic air gap flux axes. It should be mentioned that the misalignment is more sensitive for the machine with larger rotor leakage inductance, especially for the machine with open slots rotor.

For traditional method II, the command slips frequencies under no-load and rated load conditions are shown in Fig. 15. The fundamental and harmonic slips are kept zero under no-load and deviate from each other under heavy load condition. The command third harmonic slip is obtained based on the assumption that the third harmonic rotor flux orients with the command d_3-axis. As illustrated in Section II, the actual third harmonic slip is restricted to equal with the fundamental one, which is contradictory with the command value. Therefore, the actual

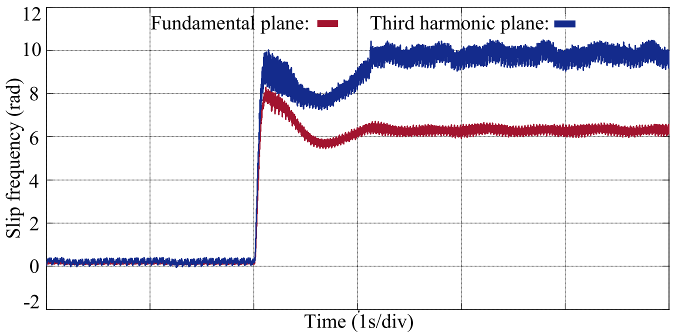

Fig. 15. Comparison for the fundamental and harmonic command slip frequencies of traditional method II.

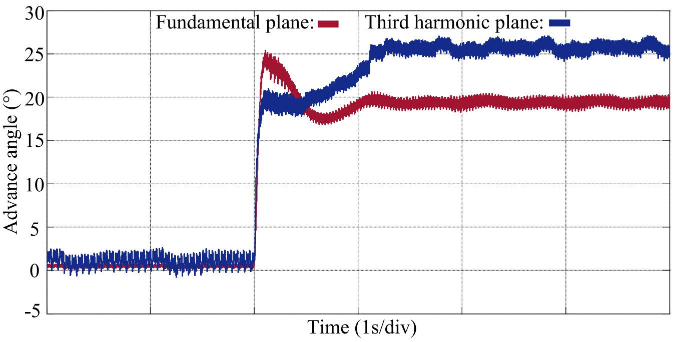

Fig. 16. Comparison for the fundamental and the actual harmonic advance angles of traditional method II.

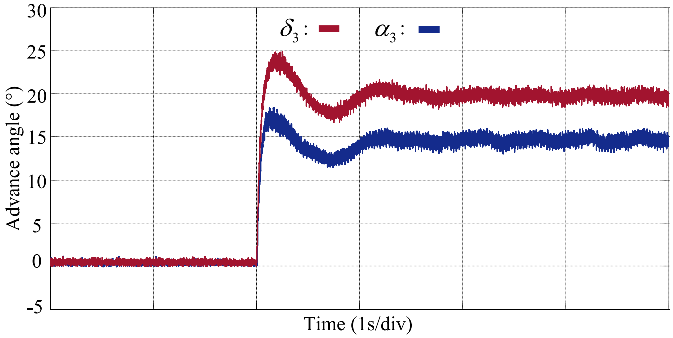

Fig. 17. Comparison of the angle alpha 3 and beta 3 for the proposed method.

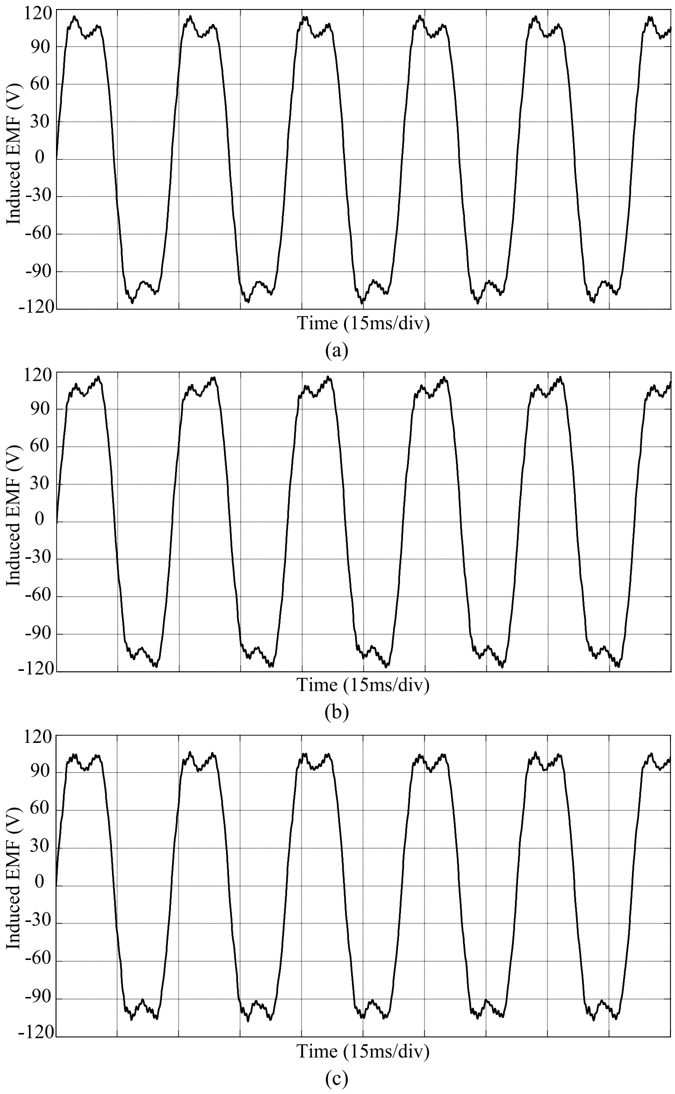

Fig. 18. Comparison for the measured induced EMF waveform under rated load. (a) Traditional method I. (b) Traditional method II. (c) Proposed method.

harmonic rotor flux deviates from the command axis to achieve the new balance.

The actual advance angle of third harmonic plane (18) is compared with the fundamental one in Fig. 16. The fundamental advance angle of air gap flux lags the harmonic one by about 5.8° electrical angle, which has the contrary characteristic with traditional method I. It should be emphasized that the relative position of the fundamental and harmonic air gap flux is indefinite and it depends on the rotor leakage inductance and the load currents of both the fundamental and harmonic planes.

For the proposed method, the comparison is conducted in Fig. 17 for the angle α_3, which lies between air gap flux and rotor flux, and the angle δ_3, which lies between air gap flux and d_1-axis. The directions of air gap flux and rotor flux are the same and along with d_1-axis under no-load, while the third harmonic rotor flux deviates from d_1-axis under heavy load condition. The d_3-axis in third harmonic plane is fixed on the axis of third harmonic air gap flux and the third harmonic advance angle δ_3 is given by tripling the fundamental advance angle δ_1, so that the constraint (6) for the advance angle can be strictly met under arbitrary load torque. The direction for the axis of third harmonic rotor flux varies with load conditions and the deflected angles relative to d_1-axis depend on the rotor leakage flux linkage.

The waveforms of induced EMF under rated load condition measured by the search coil and then processed by lowpass filter are shown in Fig. 18. The waveforms for the traditional methods I and II are distorted due to the misaligned angles between fundamental and harmonic air gap flux. The left peak of the waveforms for traditional method I is undesirably increased by around 9.5% comparing with the nominal value, whereas the right peak of the waveforms for traditional method II is higher than the normal value by around 10.6%. The quantitative indexes

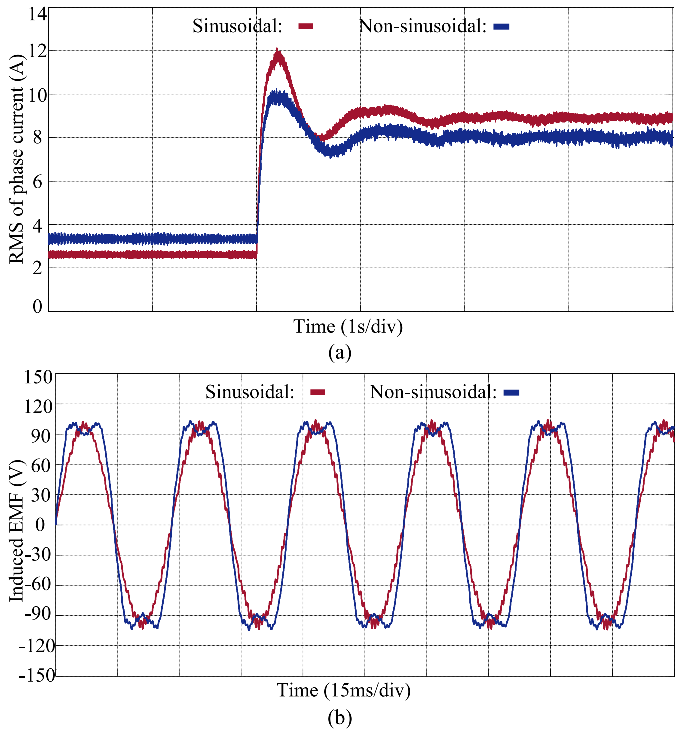

Fig. 19. Comparisons for the sinusoidal and nonsinusoidal power supply. (a) RMS of phase current. (b) waveform of the induced EMF.

are provided based on the laboratorial prototype machine, which are not definitive for other types of multiphase IMs. The misalignment between the fundamental and harmonic air gap flux will become severe for the machine with heavier load torque and larger difference between the fundamental and harmonic rotor leakage inductance. The optimal flat-topped waveforms of induced EMF can be obtained by using the proposed harmonic currents injecting algorithm, which indicates that the undesirable misaligned angle can be eliminated effectively.

The rms currents from no-load to rated load are depicted in Fig. 19(a). Under no-load condition, the rms current is higher for sinusoidal power supply in comparison with the nonsinusoidal power supply due to the additional harmonic magnetizing currents. Under rated load condition, the rms current for the proposed nonsinusoidal power supply strategy is reduced by 10.5% when comparing with the sinusoidal power supply. The waveforms of induced EMF under heavy load condition are compared for sinusoidal and nonsinusoidal power supply in Fig. 19(b). The amplitudes of induced EMF under nonsinusoidal power supply can be restricted to the same level with no salient peak relative to the waveforms of sinusoidal power supply.

V. CONCLUSION

The simulated analyses for misaligned angles reveal that the optimal distribution of air gap flux density cannot be acquired under arbitrary load torque and rotor leakage flux through the traditional rotor flux-oriented methods. It has been confirmed that the harmonic rotor flux axis will deviate from the axis of fundamental rotor flux axis (d_1-axis) under heavy load when the constraints for advance angles and slip frequencies are achieved simultaneously. For the proposed nonsinusoidal power supply strategy, AFOC is applied on harmonic planes to acquire the universal applicability that the fundamental and harmonic air gap flux strictly align with each other irrespective of load condition and rotor leakage flux linkage.

Experimental qualitative analysis and quantitative indexes are provided for the misaligned angles and the amplitudes of induced EMF in traditional methods. The experimental studies show the ideal quasi-trapezoidal waveforms in induced EMF are obtained through the proposed method, which indicates the misalignment between fundamental and harmonic air gap flux axes can be effectively avoided under heavy load condition. The RMS current and induced EMF waveforms have been compared for sinusoidal power supply and the proposed nonsinusoidal power supply strategies, and then a conclusion can be drawn that the RMS current can be reduced by 10.5% under heavy load condition without increasing the amplitude of any point in the distributed air gap flux density.

ACKNOWLEDGMENT

The experimental works are supported by the Engineering Innovation and Training Center in Polytechnic Institute of Zhejiang University.

REFERENCES

[1] E. Levi, R. Bojoi, F. Profumo, H. A. Toliyat, and S. Williamson, “Multiphase induction motor drives—A technology status review,” *IET Elect. Power Appl.*, vol. 1, no. 4, pp. 489–516, Jul. 2007.

[2] E. Levi, “Multiphase electric machines for variable-speed applications,” *IEEE Trans. Ind. Electron.*, vol. 55, no. 5, pp. 1893–1909, May 2008.

[3] F. Barrero, and M. J. Duran, “Recent advances in the design, modeling, and control of multiphase machines—Part I,” *IEEE Trans. Ind. Electron.*, vol. 63, no. 1, pp. 449–458, Jan. 2016.

[4] M. J. Duran and F. Barrero, “Recent advances in the design, modeling, and control of multiphase machines—Part II,” *IEEE Trans. Ind. Electron.*, vol. 63, no. 1, pp. 459–468, Jan. 2016.

[5] A. Tani, M. Mengoni, L. Zarri, G. Serra, and D. Casadei, “Control of multiphase induction motors with an odd number of phases under open-circuit phase faults,” *IEEE Trans. Power Electron.*, vol. 27, no. 3, pp. 565–577, Feb. 2012.

[6] J. Sun, Z. Liu, Z. Zheng, and Y. Li, “An online global fault-tolerant control strategy for symmetrical multiphase machines with minimum losses in full torque production range,” *IEEE Trans. Power Electron.*, vol. 35, no. 3, pp. 2819–2830, Mar. 2020.

[7] A. Negahdari, A. G. Yepes, J. Doval-Gandoy, and H. A. Toliyat, “Efficiency enhancement of multiphase electric drives at light-load operation considering both converter and stator copper losses,” *IEEE Trans. Power Electron.*, vol. 34, no. 2, pp. 1518–1525, Feb. 2019.

[8] Z. Liu, Y. Li, and Z. Zheng, “A review of drive techniques for multiphase machines,” *CES Trans. Elect. Mach. Syst.*, vol. 2, no. 2, pp. 243–251, Jun. 2018.

[9] R. O. C. Lyra and T. A. Lipo, “Torque density improvement in a six-phase induction motor with third harmonic current injection,” *IEEE Trans. Ind. Appl.*, vol. 38, no. 2, pp. 1351–1360, Sep./Oct. 2002.

[10] L. A. Pereira, S. Haffner, L. F. A. Pereira, and R. S. da Rosa, “Torque capability of high phase induction machines with sinusoidal and trapezoidal airgap field under steady state,” in *Proc. 39th Annu. Conf. IEEE Ind. Electron. Soc.*, 2013, vol. 1, pp. 3183–3188.

[11] A. S. Abdel-Khalik, M. Masoud, and W. Barry, “Eleven-phase induction machine: Steady-state analysis and performance evaluation with harmonic injection,” *IET Elect. Power Appl.*, vol. 4, no. 8, pp. 670–685, Sep. 2010.

[12] M. Mengoni, L. Zarri, A. Tani, L. Parsa, G. Serra, and D. Casadei, “High-torque-density control of multiphase induction motor drives operating over a wide speed range,” *IEEE Trans. Ind. Electron.*, vol. 62, no. 2, pp. 814–825, Feb. 2015.

[13] M. J. Duran, F. Salas, and M. R. Arahal, “Bifurcation analysis of five-phase induction motor drives with third harmonic injection,” *IEEE Trans. Ind. Electron.*, vol. 55, no. 5, pp. 2006–2014, May 2008.

[14] A. S. Abdel-Khalik, S. M. Gadoue, M. I. Masoud, and B. W. Wiliams, “Optimum flux distribution with harmonic injection for a multiphase induction machine using genetic algorithms,” *IEEE Trans. Energy Conv.*, vol. 26, no. 2, pp. 501–512, Jun. 2011.

[15] A. S. Abdel-Khalik, M. I. Masoud, S. Ahmed, and A. M. Massoud, “Effect of current harmonic injection on constant rotor volume multiphase induction machine stators: A comparative study,” *IEEE Trans. Ind. Appl.*, vol. 48, no. 6, pp. 2002–2013, Nov./Dec. 2012.

[16] W. Kong, J. Huang, R. Qu, M. Kang, and J. Yang, “Non-sinusoidal power supply analysis for concentrated full pitch winding multiphase induction motor,” *IEEE Trans. Ind. Electron.*, vol. 63, no. 1, pp. 574–582, Jan. 2016.

[17] W. Kong, R. Qu, M. Kang, J. Huang, and L. Jing, “Air-gap and yoke flux density optimization for multiphase induction motor based on novel harmonic current injection method,” *IEEE Trans. Ind. Appl.*, vol. 53, no. 3, pp. 2140–2148, May/Jun. 2017.

[18] H. Xu, H. A. Toliyat, and L. J. Petersen, “Five-phase induction motor drives with DSP-based control system,” *IEEE Trans. Power Electron.*, vol. 17, no. 4, pp. 524–533, Mar. 2002.

[19] C. C. Scharlau, L. F. A. Pereira, L. A. Pereira, and S. Haffner, “Performance of a five-phase induction machine with optimized air gap field under open loop V/f control,” *IEEE Trans. Energy Conv.*, vol. 23, no. 4, pp. 1046–1056, Dec. 2008.

[20] L. A. Pereira, C. C. Scharlau, L. F. A. Pereira, and S. Haffner, “Influence of saturation on the airgap induction waveform of five-phase induction machines,” *IEEE Trans. Energy Conv.*, vol. 27, no. 1, pp. 29–41, Mar. 2012.

[21] A. S. Abdel-Khalik, M. I. Masoud, and B. W. Williams, “Vector controlled multiphase induction machine: Harmonic injection using optimized constant gains,” *Electric Power Syst. Res.*, vol. 89, pp. 116–128, Aug. 2012.

[22] L. Zheng, J. E. Fletcher, B. W. Williams, and X. He, “Dual-plane vector control of a five-phase induction machine for an improved flux pattern,” *IEEE Trans. Ind. Electron.*, vol. 55, no. 5, pp. 1996–2005, May 2008.

[23] A. S. Abdel-Khalik, M. I. Masoud, and B. W. Williams, “Improved flux pattern with third harmonic injection for multiphase induction machines,” *IEEE Trans. Power Electron.*, vol. 27, no. 3, pp. 1563–1578, Mar. 2012.

[24] L. A. Pereira, C. C. Scharlau, L. F. A. Pereira, and J. F. Haffner, “General model of a five-phase induction machine allowing for harmonics in the air gap field,” *IEEE Trans. Energy Convers.*, vol. 21, no. 4, pp. 891–899, Dec. 2006.

[25] A. S. Abdel-Khalik, M. I. Daoud, S. Ahmed, A. A. Elserougi, and A. M. Massoud, “Parameter identification of five-phase induction machines with single layer windings,” *IEEE Trans. Ind. Electron.*, vol. 61, no. 10, pp. 5139–5154, Dec. 2014.

Yan Wang was born in Heilongjiang, China, in 1988. He received the B.Sc. and M.Sc. degrees in electric engineering from the Harbin University of Science and Technology, Heilongjiang, China, in 2011 and 2014, respectively. He is currently working toward the Ph.D. degree in electrical engineering with the College of Electrical Engineering of Zhejiang University, Hangzhou, China.

His research interests focus on the machine parameter identification, multiphase machine design, multiphase machine, and multiphase inverter control technology.

Jiaqiang Yang (Member, IEEE) was born in Jiangsu, China, in 1970. He received the Ph.D. degree in electrical engineering from Zhejiang University, Hangzhou, China, in 2004.

Since 2004, he has worked as a Lecturer, an Associate Professor, and a Professor with the College of Electrical Engineering, Zhejiang University. From 2012 to 2013, he was a Research Fellow with the College of Electrical and Computer, National University of Singapore, Singapore, where he is currently a Professor. His research interests include active power filters, flywheel energy storage systems, and the design and control of motor for electrical vehicle.

Guanghui Yang was born in Shanxi, China, in 1997. He received the B.Sc. degree in electrical engineering from Southeast University, Nanjing, China, in 2019. He is currently working toward the Ph.D. degree in electrical engineering with the College of Electrical Engineering, Zhejiang University, Hangzhou, China.

His current research focuses on multiphase induction motor and multiphase inverter control technology.

Sheng Li was born in Shanxi, China, in 1994. He received the M.Sc. degree in vehicle engineering from South China Agricultural University, Guangdong, China, in 2018. He is currently working toward the Ph.D. degree with Zhejiang University, Hangzhou, China.

His current research focuses on the advanced control technology for multiphase machines.

Rongfeng Deng was born in Jiangsu, China, in 1996. He received the B.Sc. degree in electrical engineering from the Wuhan University of Technology, Wuhan, China, in 2018. He is currently working toward the Ph.D. degree with the College of Electrical Engineering, Zhejiang University, Hangzhou, China.

His current research focuses on PMSM motor drives, in particular, the PMSM drive system with reduced dc capacitance.